

# SuperGS: Consistent and Detailed 3D Super-Resolution Scene Reconstruction via Gaussian Splatting

Shiyun Xie

School of Artificial Intelligence,  
Beihang University  
Beijing, China  
xieshiyun@buaa.edu.cn

Xu Wang

School of Artificial Intelligence,  
Beihang University  
Beijing, China  
21421012@buaa.edu.cn

Zhiru Wang

Sino-French Engineer School,  
Beihang University  
Beijing, China  
19241085@buaa.edu.cn

Yinghao Zhu

School of Artificial Intelligence,  
Beihang University  
Beijing, China  
zhuyinghao@buaa.edu.cn

Chengwei Pan\*

School of Artificial Intelligence,  
Beihang University  
Beijing, China  
pancw@buaa.edu.cn

Xiwang Dong

Institute of Unmanned System,  
Beihang University  
Beijing, China  
xwdong@buaa.edu.cn

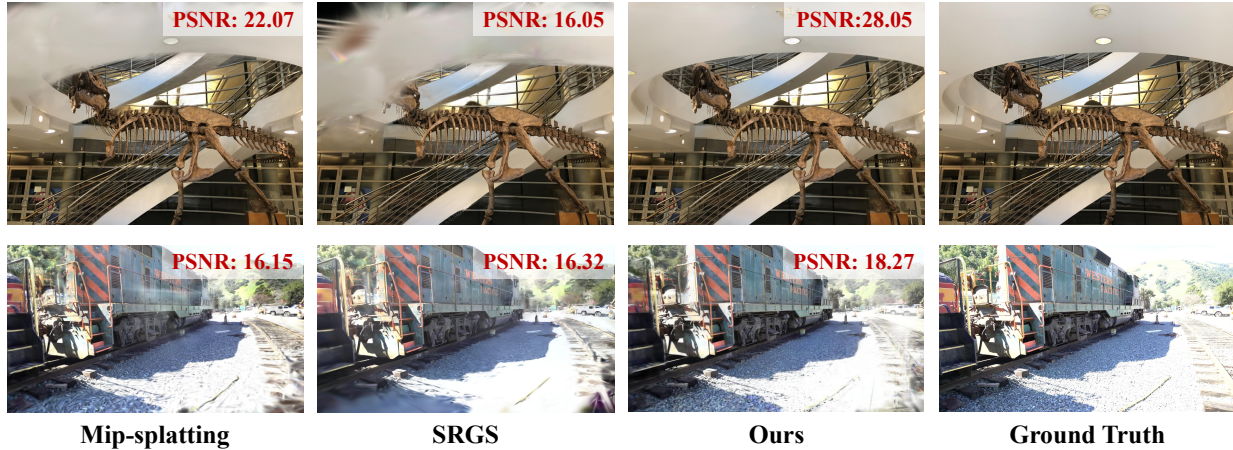


**Figure 1: Comparisons in High-resolution Novel View Synthesis.** SuperGS demonstrates more detailed and high-fidelity results compared to existing GS-based methods, delivering consistent advantages in extremely challenging scenes.

## Abstract

Recently, 3D Gaussian Splatting (3DGS) has excelled in novel view synthesis (NVS) with its real-time rendering capabilities and superior quality. However, it encounters challenges for high-resolution novel view synthesis (HRNVS) due to the coarse nature of primitives derived from low-resolution input views. To address this issue, we propose SuperGS, an expansion of Scaffold-GS designed with a two-stage coarse-to-fine training framework. In the low-resolution stage, we introduce a latent feature field to represent the low-resolution scene, which serves as both the initialization and foundational information for super-resolution optimization. In the high-resolution stage, we propose a multi-view consistent densification strategy that backprojects high-resolution depth maps based on error maps and employs a multi-view voting mechanism, mitigating ambiguities caused by multi-view inconsistencies in the pseudo labels provided by 2D prior models while avoiding Gaussian redundancy. Furthermore, we model uncertainty through variational feature learning and use it to guide further scene representation

refinement and adjust the supervisory effect of pseudo-labels, ensuring consistent and detailed scene reconstruction. Extensive experiments demonstrate that SuperGS outperforms state-of-the-art HRNVS methods on both forward-facing and 360-degree datasets.

## CCS Concepts

- Computing methodologies → Reconstruction.

## Keywords

neural rendering, computer graphics, 3D Reconstruction, super-resolution

## 1 Introduction

Novel view synthesis (NVS) is crucial for applications like AR/VR, autonomous navigation, and 3D content creation in the field of computer vision and graphics [8, 37, 45]. Traditional methods using meshes and points often sacrifice rendering quality for higher speed [3, 35, 56]. Conversely, Neural Radiance Fields (NeRF) [1, 2, 33] have significantly advanced these tasks by implicitly modeling scene geometry and radiance, but their high computational

\*Corresponding authors

demands restrict their application in real-time scenarios [4, 14, 34]. Recently emerging as a promising approach, 3D Gaussian Splatting (3DGS) [20] leverages 3D Gaussian primitives and a differentiable rasterization process for real-time, high-quality rendering. This technique eliminates the need for extensive ray sampling and incorporates clone-and-split strategies to improve spatial coverage and enhance scene representation.

However, when handling high-resolution novel view synthesis (HRNVS), vanilla 3DGS suffers from significant performance degradation. Unlike NeRF-style models, which can sample the color and opacity of any point due to their continuous implicit scene representations, 3DGS cannot directly upsample Gaussian primitives. Existing methods typically use 2D priors to guide high-resolution scene optimization. The straightforward approach is to leverage image super-resolution models to generate pseudo-labels [13], but processing images individually introduces multi-view inconsistencies. Some works propose using video super-resolution (VSR) models to ensure consistency. For example, Supergaussian [43] utilizes low-resolution reconstruction results to render continuous trajectories as videos, but this amplifies errors from the low-resolution reconstruction and offers no mechanism for correction. Sequence Matters [23] leverages the similarity between input views to obtain "video-like" sequences, but this requires dense inputs with small angular differences, limiting its practical applications. Considering the greater availability and abundance of image data, current image models possess superior feature extraction and detail restoration capabilities, while video models comparatively demand higher computational resources. Therefore, we opt to utilize a pretrained single image super-resolution (SISR) model to generate high-resolution input views as pseudo labels to guide detail enhancement.

To mitigate pseudo-label errors and achieve high-quality high-resolution reconstruction, we introduce SuperGS. This method employs a coarse-to-fine framework to ensure high fidelity, while proposing improved densification and uncertainty-aware learning strategies that simultaneously preserve reconstruction details and consistency. Due to Scaffold-GS's excellent novel view synthesis performance and low memory requirements, which are significant advantages when representing high-resolution scenes, we select it as our backbone. Scaffold-GS incorporates implicit representations into 3D Gaussian Splatting, enabling us to learn scene representations at the latent feature level rather than through explicit color and shape parameters. We further enhance Scaffold-GS by introducing a latent feature field to represent the low-resolution scene, serving as both the initialization and foundation for super-resolution optimization.

Furthermore, due to multi-view inconsistencies, gradient-based densification tends to generate excessive Gaussians to fit each training view, resulting in an overabundance of Gaussians and performance degradation in novel view synthesis. To address this, we introduce a multi-view voting densification strategy, replacing the original anchor growth policy of Scaffold-GS. This method generates candidate points based on pixel-wise loss and upsampled high-resolution depth map backprojection, then determines anchor growth through a multi-view voting mechanism, ensuring multi-view consistency while avoiding Gaussian redundancy. Additionally, we model uncertainty by learning variational features,

which help identify regions where the model lacks confidence. Subsequently, we leverage this uncertainty to further enhance the scene representation and adjust the supervision from pseudo-labels.

To evaluate the effectiveness of our method, we conducted extensive experiments on the challenging real-world and LLFF datasets. Experimental results validate that our method consistently outperforms existing methods, achieving consistent and detailed 3D super-resolution scene reconstruction in complex environments.

In summary, the main contributions of our approach are as follows :

- *Insightfully*, we introduce SuperGS, an expansion of Gaussian Splatting for 3D scene super-resolution. SuperGS incorporates 2D priors to guide detail enhancement while ensuring multi-view consistency and high-fidelity reconstruction.
- *Methodologically*, we incorporate a latent feature field throughout our two-stage coarse-to-fine framework, which enables effective information propagation. Additionally, the multi-view consistent densification and uncertainty-aware learning strategy further ensure 3D consistent and detailed super-resolution scene reconstruction.
- *Experimentally*, extensive experiments demonstrate that SuperGS consistently surpasses state-of-the-art methods on both forward-facing datasets and 360-degree datasets.

## 2 Related Work

### 2.1 Novel View Synthesis

Novel view synthesis (NVS) is a complex task in computer vision, aimed at generating new viewpoint images from a set of posed photos. Neural radiance fields (NeRF) [33] have excelled in NVS, encoding scene details into a MLP for volume rendering. However, NeRF's limitations in detail capture and efficiency led to the development of Mip-NeRF [1] and InstantNGP [34], which enhance both aspects. Subsequent research [16, 29, 30] has focused on finding a balance between rendering quality and efficiency, a persistently challenging task.

The recent development of 3D Gaussian Splatting (3DGS) [20] offers a potential solution to overcome the limitations of NeRF. By converting scene point clouds into anisotropic Gaussian primitives following Structure from Motion (SFM) [40], 3DGS uses these primitives for explicit scene representation and employs a differentiable rasterizer for real-time, high-quality rendering. Subsequent 3DGS improvements have either enhanced reconstruction quality through anti-aliasing [52, 58] and depth regulation [7, 26, 46], or focused on model compression [6, 24, 36]. Additionally, some works [31, 38] have incorporated implicit representations into 3DGS, improving performance while significantly reducing memory requirements. Various adaptations have also tailored 3DGS to specific scenarios such as sparse view reconstruction [11, 51, 62], spectacular scene reconstruction [49, 53], and dynamic scenes [10, 19, 54].

### 2.2 3D Scene Super-Resolution

High-resolution novel view synthesis (HRNVS) aims to generate high-resolution novel views from low-resolution inputs. NeRF-SR [47] addresses this by sampling multiple rays per pixel and applying regularization at the sub-pixel level. However, it requires

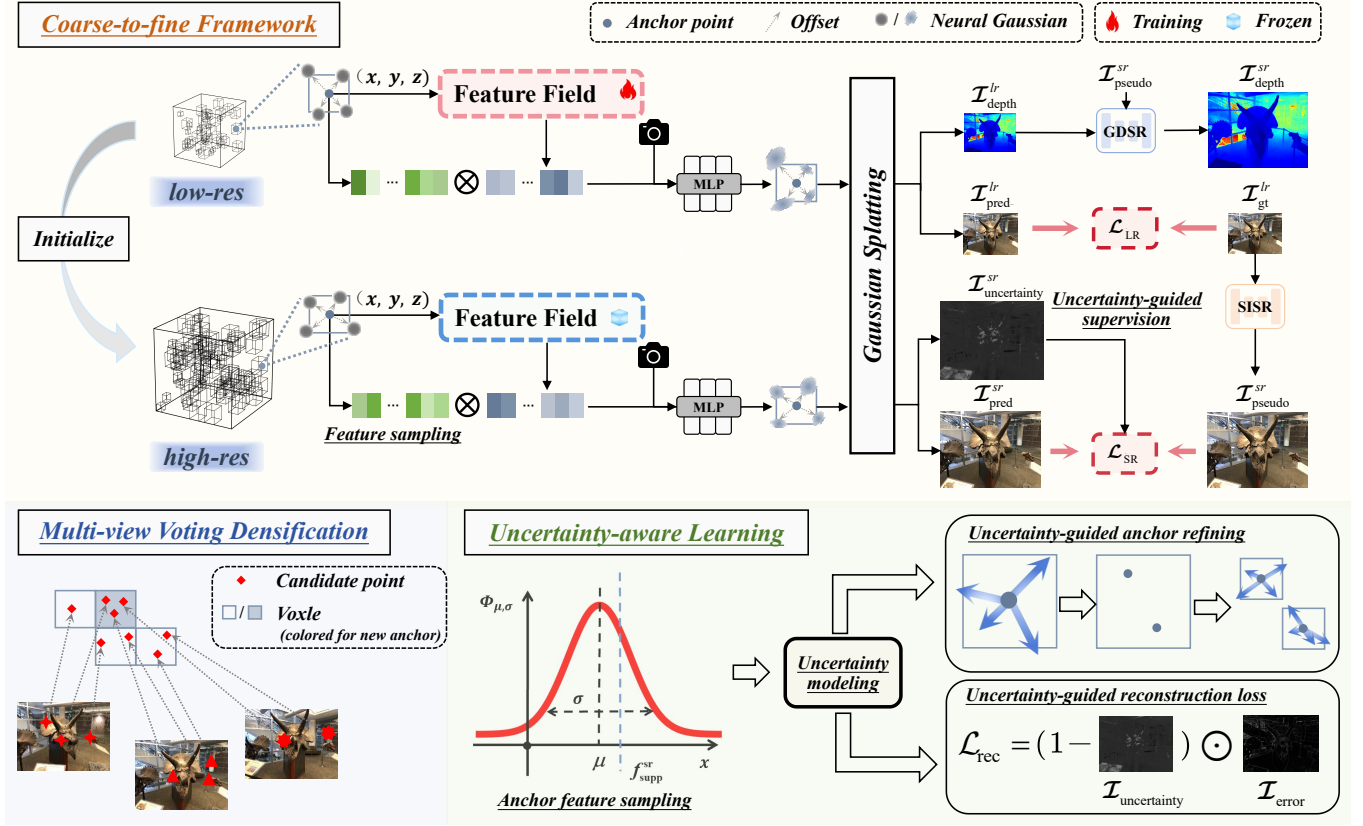


**Figure 2: Framework of our proposed SuperGS.** (a) We propose a two-stage coarse-to-fine framework. We enhance Scaffold-GS by introducing a latent feature field to represent the low-resolution scene, which serves as both initialization and foundational information for super-resolution optimization. (b) In the high-resolution stage, we propose a multi-view consistent densification strategy that replaces the original gradient-based densification, avoiding overfitting and Gaussian redundancy. (c) We model anchor uncertainty through learning variational features, which is further used to guide scene representation refinement and reconstruction loss computation.

ground truth high-resolution images as input, which are often unavailable in practical scenarios. RefSR-NeRF [18] faces similar limitations. FastSR-NeRF [28] introduces Random Patch Sampling to accelerate the process, which is crucial for high-resolution scenes. Furthermore, pretrained 2D models provide valuable priors for 3D super-resolution tasks. To ensure multi-view consistency, [57] employs cross-guided optimization, while DiSR-NeRF [25] utilizes iterative 3D synchronization and enhances image details through Renoised Score Distillation.

To ensure real-time rendering, recent work has begun exploring 3D Gaussian Splatting (3DGS) for HRNVS tasks. SRGS [13] uses high-resolution outputs from SISR as pseudo labels and introduces sub-pixel constraints as regularization. However, since image models process each input view independently, this introduces multi-view inconsistencies. SuperGaussian [43] attempts to address this by sampling smooth trajectories from 3D scenes to generate videos, then using pretrained video super-resolution (VSR) models for supervision. However, since the rendered continuous video comes

from low-resolution reconstruction rather than ground truth, up-sampling amplifies reconstruction errors without correcting them. GaussianSR faces similar issues, using low-resolution rendered images as conditions for the 2D super-resolution model StableSR [48]. Sequence Matters [23] addresses this by measuring input view similarity to generate "video-like" sequences, but requires dense inputs with small angular differences, limiting practical applications. Since images are more readily available than videos, existing 2D image models still offer superior feature representation and detail recovery, while video models require more computational resources. Therefore, we still rely on SISR models as 2D priors. We propose a coarse-to-fine framework to ensure high fidelity, along with improved densification strategies and uncertainty-aware learning to guarantee multi-view consistency.

### 3 Preliminaries

#### 3.1 3DGS

3D Gaussian Splatting (3DGS) [20] models scenes using anisotropic 3D Gaussians and renders images by rasterizing their projected 2D

counterparts. Each 3D Gaussian  $\mathcal{G}(x)$  is parameterized by a center position  $\mu \in \mathbb{R}^3$  and a covariance matrix  $\Sigma \in \mathbb{R}^{3 \times 3}$ :

$$\mathcal{G}(x) = e^{-\frac{1}{2}(x-\mu)^T \Sigma^{-1}(x-\mu)} \quad (1)$$

The covariance matrix  $\Sigma$  is parameterized through a scaling matrix  $S \in \mathbb{R}^3$  and rotation matrix  $R \in \mathbb{R}^{3 \times 3}$  with  $\Sigma = RSS^T R^T$ . Each Gaussian has associated opacity  $\sigma \in \mathbb{R}^1$  and color feature  $F \in \mathbb{R}^C$ . The rendering process employs a tile-based rasterizer that sorts 3D Gaussians in front-to-back order and projects them onto the image plane as 2D Gaussians. The color at each pixel is computed through alpha blending:

$$\hat{C} = \sum_{i \in N} c_i \alpha_i T_i \quad (2)$$

where  $N$  represents the number of sorted 2D Gaussians associated with that pixel, and  $T$  denotes the transmittance as  $\prod_{j=1}^{i-1} (1 - \alpha_j)$ .

The scene is initialized with Gaussian means and colors derived from SfM [40]. During optimization, Gaussian parameters are updated through gradient descent across multiple rendering iterations to best match the training images. At fixed intervals, the algorithm splits, clones, and prunes Gaussians based on their opacity, screen-space size, and mean gradient magnitude, respectively.

### 3.2 Scaffold-GS

Scaffold-GS [31] enhances 3D-GS by introducing a more efficient and structured primitive management system through anchors. Each anchor is associated with features that describe the local structure and emits multiple neural Gaussians:

$$\{\mu_0, \dots, \mu_{k-1}\} = X + \{O_0, \dots, O_{k-1}\} \cdot S \quad (3)$$

where  $X$  is the anchor position,  $\mu_i$  represents positions of neural Gaussians,  $O_i$  are predicted offsets, and  $S$  is a scaling factor. Properties like opacities, rotations, and colors are decoded from anchor features  $f$  through MLPs:

$$\{\alpha_0, \dots, \alpha_{k-1}\} = F_\alpha(f, \delta_{vc}, \vec{d}_{vc}) \quad (4)$$

where  $\delta_{vc}$  and  $\vec{d}_{vc}$  are relative viewing distance and direction between the camera and the anchor point.

For anchor points refinement, Scaffold-GS employs both growing and pruning operations. The growing operation adds new anchors in voxels where the gradient of neural Gaussians exceeds a threshold, allowing better representation in texture-less areas. The system quantizes space into multi-resolution voxels for adaptive refinement. Conversely, the pruning operation removes anchors that consistently produce low-opacity Gaussians, maintaining computational efficiency while preserving visual quality.

## 4 Method

In this work, we introduce a Super-Resolution Gaussian Splatting method (SuperGS) for high-resolution novel view synthesis (HRNVS) from low-resolution input views, utilizing a two-stage coarse-to-fine training framework. In coarse stage training, we obtain a rough scene representation using low-resolution ground-truth images, while in fine stage training, we enhance the details by leveraging high-resolution pseudo-labels generated from a pre-trained Single Image Super-Resolution (SISR) model [27]. The two-stage process is described as follows.

### 4.1 Coarse-to-fine Framework

**4.1.1 Hash-grid latent feature field.** The framework of SuperGS is shown in Figure 2. Our method is based on Scaffold-GS, first utilizing low-resolution ground truth images to obtain low-resolution reconstruction representation through Scaffold-GS. The key difference is that we decompose the anchor feature  $f$  into two parts:  $f_{\text{field}} \otimes f_{\text{supp}}$ , which is subsequently decoded to neural Gaussians attributes.

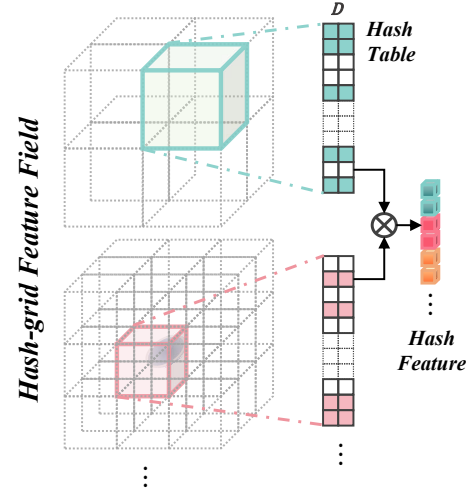


**Figure 3: Illustration of Feature Field.** For a specific anchor, we extract and interpolate features from hash tables using its coordinates, with the concatenation of features from  $L$  resolution levels forming the field feature  $f_{\text{field}}$  of this anchor.

Within this approach,  $f_{\text{field}}$  is derived from a latent feature field, which learns low-resolution scene information and serves as the foundational feature for subsequent high-resolution stage. Drawing inspiration from InstantNGP [34], we adopt a similar strategy by storing view-independent features in multi-resolution grids. This approach allows for efficient access to anchor features at arbitrary positions by indexing through hash tables followed by linear interpolation. For each anchor, we retrieve learnable feature vectors stored in grids with varying resolutions and perform linear interpolation to derive its feature representation. Notably, different levels of grids correspond to distinct hash tables. Specifically, there are  $L$  levels of grid resolutions, and the feature vector interpolated for the  $i$ -th anchor at the  $l$ -th level is denoted as  $f_{\text{field}}^{(l)}$ . From this, we construct its multi-resolution feature vector representation as follows:

$$f_{\text{field}} = f_{\text{field}}^{(1)} \otimes f_{\text{field}}^{(2)} \otimes \dots \otimes f_{\text{field}}^{(L)} \quad (5)$$

where  $\otimes$  denotes the concatenation operation.

Similarly, to enable the grid feature field to extend to unbounded scenes, we reference the approach used in Mip-NeRF360 [1], which normalizes the coordinates of the anchors into a contracted space. The contraction is formally described as follows:

$$\text{contract}(X_i) = \begin{cases} X_i, & \|X_i\| \leq 1 \\ (2 - \frac{1}{\|X_i\|})(\frac{X_i}{\|X_i\|}), & \|X_i\| > 1 \end{cases} \quad (6)$$

where  $X_i \in \mathbb{R}^3$  represents the position coordinate of  $i$ -th anchor.

Since  $f_{\text{field}}$  is interpolated from the feature field based on anchor positions, inevitably resulting in some information loss, we retain a low-dimensional learnable feature  $f_{\text{supp}}^{\text{lr}}$  at each anchor to supplement the missing information. Then, followed by Scaffold-GS, the neural Gaussians attributes  $\alpha$ ,  $q$ ,  $s$  and  $c$  are decoded by anchor feature. For example, opacity values of neural Gaussians spawned from an anchor point are given by:

$$\{\alpha_0, \dots, \alpha_{k-1}\} = F_{\alpha}(f_{\text{field}}, f_{\text{supp}}^{\text{lr}}, \delta_{vc}, \bar{d}_{vc}), \quad (7)$$

**4.1.2 Variational anchor feature.** During the fine training stage, we freeze the parameters of the feature field, and use the interpolated feature  $f_{\text{field}}$  obtained through position indexing as the base feature. Additionally, we still attach a learnable feature vector  $f_{\text{supp}}^{\text{sr}}$  to each anchor to enhance high-resolution details, which is initialized by the low-resolution feature  $f_{\text{supp}}^{\text{lr}}$ .

Since we utilize a 2D pretrained SISR model to obtain high-resolution pseudo-labels, multi-view inconsistencies can lead to ambiguity during model training. Therefore, we model  $f_{\text{field}}^{\text{sr}}$  as a variational feature for representing the uncertainty of each anchor, which subsequently guides anchor refinement and loss computation as described in Section 4.3. Specifically, we assume that  $f_{\text{supp}}^{\text{sr}}$  follows a normal distribution  $\mathcal{N}(f_{\mu}, \exp(f_{\sigma}))$ , learning both the mean and variance, where the exponential operation ensures the variance is non-negative. To achieve forward propagation and ensure that gradients can backpropagate, we use the reparameterization trick [21] for feature sampling:

$$f_{\text{supp}}^{\text{sr}} = f_{\mu} + \epsilon \cdot \exp(f_{\sigma}), \quad \epsilon \sim \mathcal{N}(0, 1) \quad (8)$$

where  $f_{\mu}$  is initialized by  $f_{\text{supp}}^{\text{lr}}$ , and  $f_{\sigma}$  is initialized with very small values.

Unlike previous two-stage methods [12, 17, 43], which only utilize low-resolution reconstruction as initialization for high-resolution reconstruction, our method establishes a latent feature field that represents the low-resolution 3D scene, serving as the foundational feature for the high-resolution representation. This approach not only provides an initial coarse feature for high-resolution anchors in the subsequent fine-stage training but also ensures that additional details remain consistent with the core scene information. This guarantees high fidelity in the high-resolution scene reconstruction while mitigating the impact of errors from pseudo-labels.

## 4.2 Multi-view Consistent Densification

Experiments demonstrate that during the fine training stage, using the gradient-based adaptive densification strategy from 3DGS and Scaffold-GS can degrade performance, as shown in Figure 4. This may stem from multi-view inconsistencies in pseudo-labels, requiring more Gaussians to fit texture from each viewpoint, thus causing significant deviations in novel view synthesis. Additionally, some methods [39, 60] have indicated that gradient-based densification strategies can lead to underfitting in highly textured regions, while simply lowering thresholds results in excessive Gaussian redundancy. Therefore, we combine pixel-wise errors with depth map and utilize a multi-view voting mechanism to determine anchor growth.

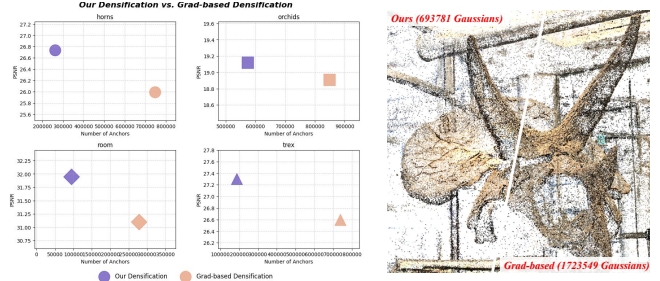


**Figure 4: Comparison of Ours Densification and Gradient-based Densification Startegy.** Our method achieves better reconstruction quality with fewer anchor points, reducing memory requirements while preventing overfitting.

**4.2.1 Depth map rendering and super-resolution.** Depth maps provide rich geometric structural information, though depth maps obtained from monocular depth estimation models often have scale inconsistencies with the actual training scene [46]. To address this, we first render low-resolution depth maps, then employ a pretrained guided depth map super-resolution (GDSR) model [50] to obtain high-resolution depth maps, which uses high-resolution RGB images to guide the upsampling of low-resolution depth maps. This approach yields high-resolution depth maps that are not only scale-matched but also consistent with geometric structure information in the pseudo-labels.

For low-resolution depth map rendering, common approaches include alpha blending or selecting the largest contributing weight  $w_i = T_i \alpha_i$  to represent the depth of each pixel. The former results in pixel depth values influenced by all Gaussians along the ray, producing smoother depth maps but lacking precise 3D structure. The latter only considers the highest-weighted Gaussian, which can be problematic in transparent scenes. Following the approach in [51], we apply softmax-scaling to optimize the original alpha blending weights during low-resolution depth map rendering:

$$d_{u,v}^{\text{lr}} = \log \left( \frac{\sum_{i=1}^N w_i e^{\beta w_i} d_i}{\sum_{i=1}^N w_i e^{\beta w_i}} \right) \quad (9)$$

The exponential term enhances the contribution of high-opacity Gaussians while reducing noise influence from low-weight Gaussians. The parameter  $\beta$  adjusts the softmax temperature, with higher values creating more pronounced weight differentiation.

**4.2.2 Error-based depth projection and multi-view voting mechanism.** The multi-view stereo (MVS) methods [5, 55, 61] utilize depth projection to point clouds for 3D reconstruction, but their depth maps typically come from sensors and can only reconstruct areas with high confidence. In contrast, we have already obtained high-quality pseudo high-resolution depth maps from Section 4.2.1, which contain excellent geometric prior information. However, pixel-level depth projection leads to over-reconstruction and brings unacceptable memory requirements for GS-based methods. Based on these considerations, we propose a multi-view consistent densification mechanism.

First, we define under-reconstruction regions as areas where the loss between rendered images and high-resolution pseudo-labels is

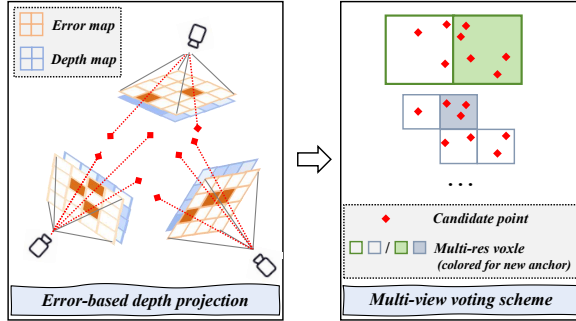


**Figure 5: Illustration of Densification Strategy.** We introduce a multi-view voting densification strategy that replaces the original anchor growing policy. First, we generate candidate Gaussian positions by back-projecting the corresponding pixels with depth map based on pixel-wise loss. Subsequently, new anchors are added when the accumulated vote count within a voxel exceeds a predetermined threshold.

large, and backproject the depth from these regions to obtain candidate Gaussian positions. Specifically, given the camera intrinsics  $K_k$  and extrinsics  $[R_k, t_k]$  for the  $k$ -th viewpoint, we can project a specific pixel coordinate  $p_{k,i} = [u_{k,i}, v_{k,i}]^T$  into 3D space using its corresponding depth value  $d_{k,i}$ , resulting in the 3D coordinate  $X_{k,i}$ :

$$X_{k,i} = R_k^T K_k^{-1} [u_{k,i} d_{k,i} \ v_{k,i} d_{k,i} \ d_{k,i}] + t_k \quad (10)$$

Retaining all projected candidate points would result in tremendous memory usage and lead to overfitting to training views, with errors becoming more pronounced when pseudo-labels are inconsistent. Therefore, we propose a multi-view voting mechanism to densify anchors in under-reconstructed regions. While Scaffold-GS defines each voxel as a unit and uses the sum of gradients of neural Gaussians within each voxel as a condition for anchor growing, we instead use the number of candidate points in each voxel as a condition for anchor densification. We treat candidate points as votes from various training viewpoints in the corresponding region and add an anchor to voxels where the point count exceeds a threshold. Similarly, we employ a multi-resolution voxel grid to allow new anchors to be added at different granularities, with regions containing more candidate points receiving anchors at higher levels.

### 4.3 Uncertainty-aware Learning

**4.3.1 Uncertainty modeling.** We leverage pseudo-labels generated by SISR models as supervision, though this approach introduces multi-view inconsistencies. To address this, we model the supplementary anchor feature  $f_{\text{supp}}^r$  as a Gaussian distribution rather than a single feature vector, as described in Section 4.1.2. The predicted variance serves as an uncertainty indicator for each anchor. Formally, we define the uncertainty  $u_i$  of the  $i$ -th anchor using the magnitude of its feature variance:

$$u_i = \|\exp(f_{\sigma})\|_2 \quad (11)$$

This uncertainty estimation allows us to identify problematic regions and implement targeted refinement strategies. Note that for the 360-degree datasets, we jointly train with three viewpoints

per iteration as in MVGS [9], which helps improve uncertainty modeling while accelerating convergence.

**4.3.2 Uncertainty-guided anchor refining.** Intuitively, high uncertainty values indicate areas where the model lacks confidence in its reconstruction. Therefore, we propose an uncertainty-guided anchor refining strategy. Specifically, anchors with uncertainty exceeding a threshold will be refined by splitting into two extra anchors, which are then added to corresponding voxels at the next level. Given an anchor located within a voxel at level  $l$ , we randomly sample two positions within this voxel and voxelize these points using the level  $l+1$  voxel size:

$$X_{\text{new}} = \left\{ \left[ \frac{X_{\text{sample}}}{\epsilon^{(l+1)}} \right] \right\} \cdot \epsilon^{(l+1)} \quad (12)$$

where  $X_{\text{sample}}$  represents the randomly sampled positions within the original voxel, and  $X_{\text{new}}$  denotes the refined voxel centers, which serve as coordinates for the new anchors. The relationship between voxel sizes at adjacent levels is defined as:

$$\epsilon^{(l+1)} = \epsilon^{(l)} / 4 \quad (13)$$

Importantly, we ensure the two sampled points maintain sufficient distance to prevent them from falling within the same voxel, achieved by generating sampling offsets in opposite directions from the original voxel center. Additionally, if a refined voxel already contains an anchor, no new anchor is added. This approach shares conceptual similarities with Gaussian Splitting scheme in 3DGS [20], as both utilize more Gaussians to refine scene representation in under-optimized regions. During both anchor densification and anchor refining stages, we employ opacity-based anchor pruning strategy of Scaffold-GS to prevent excessive anchor redundancy.

**4.3.3 Uncertainty-guided supervision.** The inconsistencies in pseudo-labels create ambiguities during model learning, resulting in increased uncertainty. We aim to reduce the influence of these inconsistent regions by weakening their supervisory role. First, we generate an uncertainty map for each view. Unlike NeRF-based methods [41, 42] that typically estimate uncertainty map through multiple sampling and rendering iterations, a highly time-consuming process, we directly render uncertainties of Gaussians via alpha blending. For the  $p$ -th pixel in the  $k$ -th view, the uncertainty  $U_{k,p}$  is calculated as:

$$U_{k,p} = \sum_{i \in N} u_i \alpha_i \prod_{j=1}^{i-1} (1 - \alpha_j) \quad (14)$$

where, for convenience, each neural Gaussian's uncertainty is assigned the value of its associated anchor's uncertainty. We then implement an uncertainty-guided reconstruction loss instead of the standard  $\mathcal{L}_1$  loss:

$$\mathcal{L}_{\text{rec}} = \|(1 - \sigma(U(u, v))) \odot (\mathcal{I}_{\text{pred}} - \mathcal{I}_{\text{pseudo}})\|_1 \quad (15)$$

where  $\sigma(\cdot)$  represents sigmoid function.

This approach ensures that regions with higher confidence in the pseudo-labels exert greater influence on parameter updates, resulting in more accurate scene representation.

**Table 1: Quantitative comparison for HRNVS ( $\times 4$ ) on real-world datasets. Mip-NeRF360:  $1/8 \rightarrow 1/2$ , Deep Blending:  $1/4 \rightarrow 1/1$ , Tanks&Temples:  $480 \times 270 \rightarrow 1920 \times 1080$ .**

Dataset Method&Metric	Mip-NeRF360				Deep Blending				Tanks&Temples			
	PSNR↑	SSIM↑	LPIPS↓	FID↓	PSNR↑	SSIM↑	LPIPS↓	FID↓	PSNR↑	SSIM↑	LPIPS↓	FID↓
3DGS	20.72	0.617	0.396	68.45	26.71	0.839	0.324	81.81	18.32	0.612	0.415	35.18
Scaffold-GS	26.15	0.739	0.316	78.25	28.36	0.872	0.306	69.55	20.50	0.667	0.396	35.54
Mip-splatting	26.42	0.756	0.294	37.73	28.85	0.884	0.282	59.44	20.65	0.672	0.385	30.25
GaussianSR	25.60	0.663	0.368	-	28.28	0.873	0.307	-	-	-	-	-
SRGS	26.88	<b>0.767</b>	<b>0.286</b>	46.37	29.40	0.894	0.272	60.96	20.70	0.687	0.379	34.58
<b>Ours</b>	<b>27.28</b>	<b>0.767</b>	0.290	<b>34.26</b>	<b>30.05</b>	<b>0.901</b>	<b>0.271</b>	<b>53.47</b>	<b>21.31</b>	<b>0.693</b>	<b>0.371</b>	<b>28.76</b>

#### 4.4 Losses Design

Following Scaffold-GS, we incorporate the SSIM loss  $\mathcal{L}_{\text{SSIM}}$  and volume regularization loss  $\mathcal{L}_{\text{vol}}$ . Unlike most super-resolution methods [13, 17, 47], we avoid directly constraining high-resolution rendered images with low-resolution ground truth images through color-based losses. Such constraints would limit the model’s ability to synthesize fine texture details and subtle high-frequency elements that are essential for realistic super-resolution. To enhance fidelity, we instead downsample the high-resolution rendered images and compute the LPIPS loss  $\mathcal{L}_{\text{LPIPS}}$  against low-resolution ground truth images, ensuring perceptual consistency across resolutions. The total supervision is given by:

$$\mathcal{L} = \mathcal{L}_{\text{rec}} + \lambda_{\text{SSIM}} \mathcal{L}_{\text{SSIM}} + \lambda_{\text{vol}} \mathcal{L}_{\text{vol}} + \lambda_{\text{LPIPS}} \mathcal{L}_{\text{LPIPS}} \quad (16)$$

### 5 Experiments

#### 5.1 Experimental Setups

**5.1.1 Datasets and metrics.** We conduct a comprehensive evaluation of our proposed model using PSNR, SSIM, LPIPS [59] and FID metrics. For LPIPS, we use VGG [44] as the backbone. Our evaluation covers 21 scenes from both real-world and synthetic datasets, including 9 scenes from Mip-NeRF360 [2], 2 scenes from Deep Blending [15], 2 scenes from Tanks&Temples [22] and 8 scenes from LLFF [32, 33]. For Mip-NeRF360 and LLFF, We downsample the training views by a factor of 8 as low-resolution inputs for the  $\times 4$  HRNVS tasks. For Deep Blending and Tanks&Temples, we downsample the training views by a factor of 4 as inputs.

**5.1.2 Baselines.** To validate the effectiveness of our method, we conduct comparisons with several prominent existing approaches. For 3DGS [20] and Scaffold-GS [31], we train using low-resolution input views and directly render high-resolution images. For Mip-splatting [58], which is a full-scale NVS method, we run the source code with its multi-resolution training setup. Regarding NeRF-SR [47] and GaussianSR [17] we directly cite the results from respective papers under the same settings. And for SRGS [13], we run the source code to obtain both qualitative and quantitative under identical conditions. Notably, to maintain fairness in the comparisons, we utilize the same pretrained SISR model, SwinIR [27] to upsample the low-resolution input views, mirroring SRGS [13].

**5.1.3 Implementation details.** We implement our framework based on the Scaffold-GS [20] source code and modify the differentiable Gaussian rasterization to include softmax-scaling depth and uncertainty rendering. For the anchor feature, we employ a 16-dimensional

feature from the latent feature field and a 16-dimensional supplementary feature bound to each anchor. In our multi-view voting densification strategy, we select pixels with loss exceeding 0.08 for reprojection, performing an anchor growth operation every 100 iterations. For anchor refinement, we iterate for 1,000 iterations following the densification process. Additionally, we train low-resolution scenes for 30,000 iterations and high-resolution scenes for 15,000 iterations. All experiments are conducted on a single RTX A6000 GPU.

#### 5.2 Experimental Results

**Table 2: Quantitative comparison for HRNVS ( $\times 4$ ) on LLFF dataset. LLFF:  $504 \times 378 \rightarrow 2016 \times 1512$ .**

Dataset Method&Metric	LLFF			
	PSNR↑	SSIM↑	LPIPS↓	FID↓
3DGS	17.55	0.547	0.448	130.31
Scaffold-GS	18.15	0.579	0.424	142.60
NeRF-SR	25.13	0.730	-	-
Mip-splatting	23.68	0.743	0.332	59.45
SRGS	23.43	0.770	0.308	61.84
<b>Ours</b>	<b>25.43</b>	<b>0.789</b>	<b>0.276</b>	<b>34.65</b>

**5.2.1 Quantitative comparison.** Tables 1 and 2 present quantitative comparison results for HRNVS tasks on real-world and LLFF datasets. On the LLFF dataset, SuperGS achieves superior performance, outperforming NeRF-SR by +0.30dB in PSNR. More significantly, SuperGS reduces the FID score to 34.65, a 41.7% improvement over Mip-Splatting, indicating more visually coherent and perceptually accurate reconstructions. Across all three real-world datasets, our method consistently delivers superior PSNR and SSIM metrics. On Deep Blending, SuperGS reaches 30.05 PSNR, surpassing SRGS by +0.65dB. Perceptual quality improvements are particularly notable, with FID reductions of 12.11 points (26.1%) on Mip-NeRF360 and 5.82 points (16.8%) on Tanks&Temples compared to the best alternative method.

**5.2.2 Qualitative comparison.** As shown in Figure 6 and 7, 3DGS and Scaffold-GS exhibits severe low-frequency artifacts due to the lack of high-resolution information, while Mip-splatting struggles with insufficient detail recovery due to missing high-frequency information. SRGS also exhibits significant artifacts and reconstruction errors. In contrast, our method demonstrates superior precision and fidelity in detail recovery while substantially reducing artifacts that severely affect the visual quality of other methods.

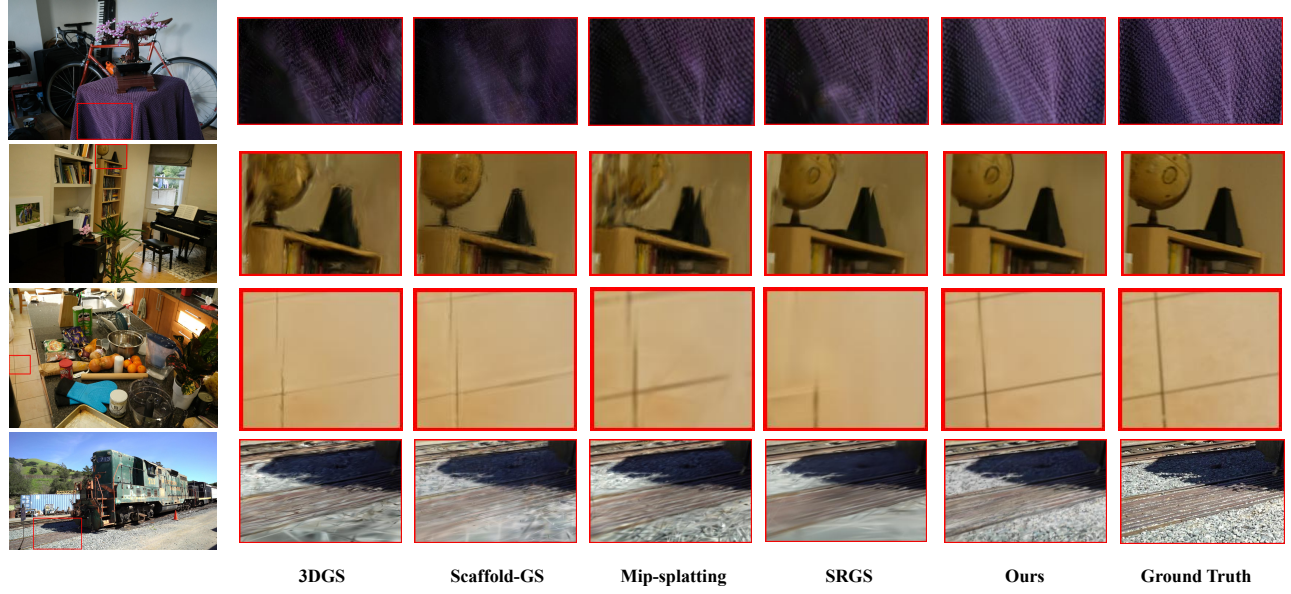


Figure 6: Qualitative comparison of the HRNVS ( $\times 4$ ) on real-world datasets. We highlight the difference with colored patches.

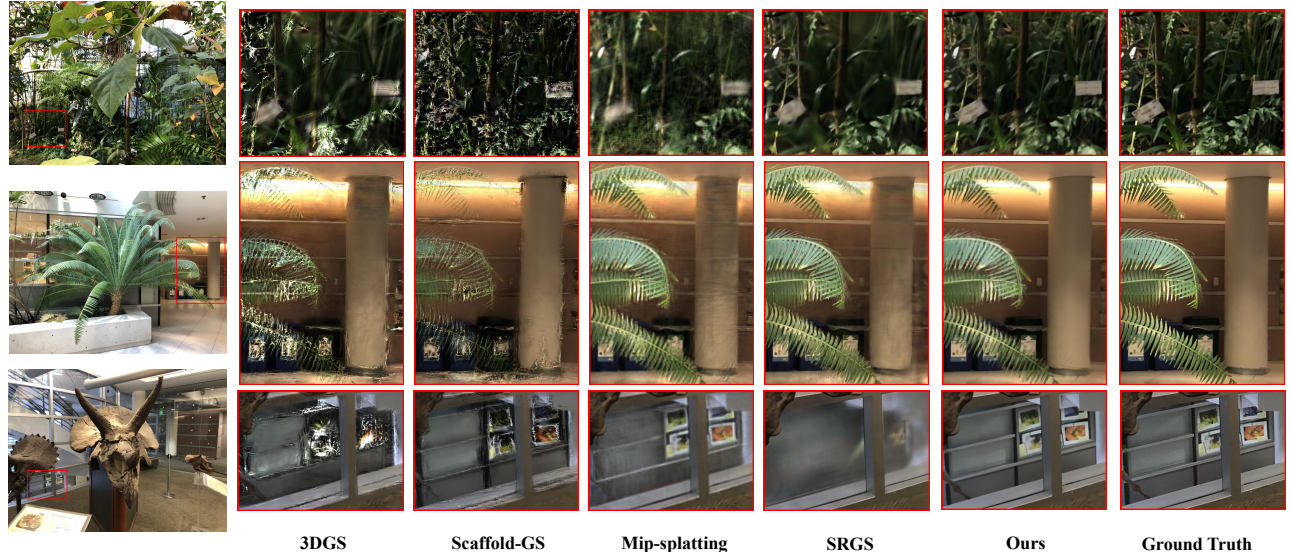


Figure 7: Qualitative comparison of the HRNVS ( $\times 4$ ) on LLFF dataset. We highlight the difference with colored patches.

### 5.3 Ablation Studies

We conduct ablation experiments on the LLFF dataset. Quantitative results are shown in Table 3.

**5.3.1 Effectiveness of latent feature field.** We evaluated two approaches: using only low-resolution anchor features as initialization for high-resolution learning, versus employing our feature field to provide foundational texture information for high-resolution learning. The latter approach demonstrated better performance, achieving a 0.15dB improvement in PSNR on the LLFF dataset.

Table 3: Ablation study results for HRNVS ( $\times 4$ ) on LLFF dataset.

Dataset Method&Metric	LLFF			
	PSNR $\uparrow$	SSIM $\uparrow$	LPIPS $\downarrow$	FID $\downarrow$
w/o Feature Field	25.28	0.786	<b>0.273</b>	39.08
w/o Densification	24.89	0.768	0.396	47.69
w/o Uncertainty	25.35	0.774	0.277	38.45
<b>Ours-full</b>	<b>25.43</b>	<b>0.789</b>	0.276	<b>34.65</b>

**5.3.2 Effectiveness of multi-view consistent densification.** We compared our proposed multi-view voting anchor densification strategy against the gradient-based anchor growth policy from Scaffold-GS [31]. Our method not only improved PSNR by 0.54dB but also required significantly fewer anchors than the gradient-based approach, as shown in Figure 4. This reduces memory requirements while preventing overfitting to pseudo training views.

**5.3.3 Effectiveness of uncertainty-aware learning.** The uncertainty-aware augmented learning module further refines scene reconstruction and mitigates the impact of pseudo-label errors. This component provides an additional 0.08dB improvement in PSNR.

## 6 Conclusion

In this work, we present SuperGS, an expansion of Gaussian Splatting for super-resolution scene reconstruction. Our method is based on a two-stage coarse-to-fine framework, introducing a latent feature field to represent the low-resolution scene, which serves as both initialization and foundational information for high-resolution reconstruction. To address the multi-view inconsistency of pseudo-labels, we introduce multi-view voting densification, ensuring consistency and effectiveness while avoiding overfitting. Additionally, we model scene uncertainty by learning variational features, which is further used to refines scene representation and guides supervision. The results consistently demonstrate the superior performance of our method on the HRNVS task.

## References

- [1] Jonathan T Barron, Ben Mildenhall, Matthew Tancik, Peter Hedman, Ricardo Martin-Brualla, and Pratul P Srinivasan. 2021. Mip-nerf: A multiscale representation for anti-aliasing neural radiance fields. In *Proceedings of the IEEE/CVF international conference on computer vision*. 5855–5864.
- [2] Jonathan T Barron, Ben Mildenhall, Dor Verbin, Pratul P Srinivasan, and Peter Hedman. 2022. Mip-nerf 360: Unbounded anti-aliased neural radiance fields. In *Proceedings of the IEEE/CVF Conference on Computer Vision and Pattern Recognition*. 5470–5479.
- [3] Mario Botsch, Alexander Hornung, Matthias Zwicker, and Leif Kobbelt. 2005. High-quality surface splatting on today’s GPUs. In *Proceedings Eurographics/IEEE VGTC Symposium Point-Based Graphics, 2005*. IEEE, 17–141.
- [4] Anpei Chen, Zexiang Xu, Andreas Geiger, Jingyi Yu, and Hao Su. 2022. TensorRF: Tensorial Radiance Fields. In *European Conference on Computer Vision (ECCV)*.
- [5] Rui Chen, Songfang Han, Jing Xu, and Hao Su. 2019. Point-based multi-view stereo network. In *Proceedings of the IEEE/CVF international conference on computer vision*. 1538–1547.
- [6] Yihang Chen, Qianyi Wu, Weiyao Lin, Mehrtash Harandi, and Jianfei Cai. 2024. Hac: Hash-grid assisted context for 3d gaussian splatting compression. In *European Conference on Computer Vision*. Springer, 422–438.
- [7] Jaeyoung Chung, Jeongtaek Oh, and Kyoung Mu Lee. 2024. Depth-regularized optimization for 3d gaussian splatting in few-shot images. In *Proceedings of the IEEE/CVF Conference on Computer Vision and Pattern Recognition*. 811–820.
- [8] Nianchen Deng, Zhenyi He, Jiannan Ye, Budmonde Duinkharjav, Praneeth Chakravarthula, Xubo Yang, and Qi Sun. 2022. Fov-nerf: Foveated neural radiance fields for virtual reality. *IEEE Transactions on Visualization and Computer Graphics* 28, 11 (2022), 3854–3864.
- [9] Xiaobiao Du, Yida Wang, and Xin Yu. 2024. Mvgs: Multi-view-regulated gaussian splatting for novel view synthesis. *arXiv preprint arXiv:2410.02103* (2024).
- [10] Yuanxing Duan, Fangyin Wei, Qiyu Dai, Yuhang He, Wenzheng Chen, and Baoquan Chen. 2024. 4d gaussian splatting: Towards efficient novel view synthesis for dynamic scenes. *arXiv preprint arXiv:2402.03307* (2024).
- [11] Zhiwen Fan, Kairun Wen, Wenyang Cong, Kevin Wang, Jian Zhang, Xinghao Ding, Danfei Xu, Boris Ivanovic, Marco Pavone, Georgios Pavlakos, Zhangyang Wang, and Yue Wang. 2024. InstantSplat: Sparse-view Gaussian Splatting in Seconds. *arXiv:2403.20309* [cs.CV]
- [12] Xiang Feng, Yongbo He, Yubo Wang, Chengkai Wang, Zhenzhong Kuang, Jiajun Ding, Feiwei Qin, Jun Yu, and Jianping Fan. 2024. ZS-SRT: An efficient zero-shot super-resolution training method for Neural Radiance Fields. *Neurocomputing* 590 (2024), 127714.
- [13] Xiang Feng, Yongbo He, Yubo Wang, Yan Yang, Zhenzhong Kuang, Yu Jun, Jianping Fan, et al. 2024. SRGS: Super-Resolution 3D Gaussian Splatting. *arXiv preprint arXiv:2404.10318* (2024).
- [14] Sara Fridovich-Keil, Alex Yu, Matthew Tancik, Qinhong Chen, Benjamin Recht, and Angjoo Kanazawa. 2022. Plenoxels: Radiance fields without neural networks. In *Proceedings of the IEEE/CVF Conference on Computer Vision and Pattern Recognition*. 5501–5510.
- [15] Peter Hedman, Julien Philip, True Price, Jan-Michael Frahm, George Drettakis, and Gabriel Brostow. 2018. Deep blending for free-viewpoint image-based rendering. *ACM Transactions on Graphics (TOG)* 37, 6 (2018), 1–15.
- [16] Peter Hedman, Pratul P Srinivasan, Ben Mildenhall, Jonathan T Barron, and Paul Debevec. 2021. Baking neural radiance fields for real-time view synthesis. In *Proceedings of the IEEE/CVF international conference on computer vision*. 5875–5884.
- [17] Jintong Hu, Bin Xia, Bin Chen, Wenming Yang, and Lei Zhang. 2024. GaussianSR: High Fidelity 2D Gaussian Splatting for Arbitrary-Scale Image Super-Resolution. *arXiv preprint arXiv:2407.18046* (2024).
- [18] Xudong Huang, Wei Li, Jie Hu, Hanting Chen, and Yunhe Wang. 2023. Refsr-nerf: Towards high fidelity and super resolution view synthesis. In *Proceedings of the IEEE/CVF Conference on Computer Vision and Pattern Recognition*. 8244–8253.
- [19] Yiming Huang, Beilei Cui, Long Bai, Ziqi Guo, Mengya Xu, and Hongliang Ren. 2024. Endo-4dgs: Distilling depth ranking for endoscopic monocular scene reconstruction with 4d gaussian splatting. *arXiv preprint arXiv:2401.16416* (2024).
- [20] Bernhard Kerbl, Georgios Kopanas, Thomas Leimkühler, and George Drettakis. 2023. 3D Gaussian Splatting for Real-Time Radiance Field Rendering. *ACM Trans. Graph.* 42, 4 (2023), 139–1.
- [21] Diederik P Kingma. 2013. Auto-encoding variational bayes. *arXiv preprint arXiv:1312.6114* (2013).
- [22] Arno Knapsitsch, Jaesik Park, Qian-Yi Zhou, and Vladlen Koltun. 2017. Tanks and temples: Benchmarking large-scale scene reconstruction. *ACM Transactions on Graphics (TOG)* 36, 4 (2017), 1–13.
- [23] Hyun-kyu Ko, Dongheok Park, Youngin Park, Byeonghyeon Lee, Juhee Han, and Eunbyung Park. 2024. Sequence Matters: Harnessing Video Models in Super-Resolution. *arXiv preprint arXiv:2412.11525* (2024).
- [24] Joo Chan Lee, Daniel Rho, Xiangyu Sun, Jong Hwan Ko, and Eunbyung Park. 2024. Compact 3d gaussian representation for radiance field. In *Proceedings of the IEEE/CVF Conference on Computer Vision and Pattern Recognition*. 21719–21728.
- [25] Jie Long Lee, Chen Li, and Gim Hee Lee. 2024. DiSR-NeRF: Diffusion-Guided View-Consistent Super-Resolution NeRF. In *Proceedings of the IEEE/CVF Conference on Computer Vision and Pattern Recognition*. 20561–20570.
- [26] Jiahe Li, Jiawei Zhang, Xiao Bai, Jin Zheng, Xin Ning, Jun Zhou, and Lin Gu. 2024. Dngaussian: Optimizing sparse-view 3d gaussian radiance fields with global-local depth normalization. In *Proceedings of the IEEE/CVF conference on computer vision and pattern recognition*. 20775–20785.
- [27] Jingyun Liang, Jiezhang Cao, Guolei Sun, Kai Zhang, Luc Van Gool, and Radu Timofte. 2021. Swinir: Image restoration using swin transformer. In *Proceedings of the IEEE/CVF international conference on computer vision*. 1833–1844.
- [28] Chien-Yu Lin, Qichen Fu, Thomas Merth, Karren Yang, and Anurag Ranjan. 2024. Fastsr-nerf: Improving nerf efficiency on consumer devices with a simple super-resolution pipeline. In *Proceedings of the IEEE/CVF Winter Conference on Applications of Computer Vision*. 6036–6045.
- [29] Haotong Lin, Sida Peng, Zhen Xu, Yunzhi Yan, Qing Shuai, Hujun Bao, and Xiaowei Zhou. 2022. Efficient neural radiance fields for interactive free-viewpoint video. In *SIGGRAPH Asia 2022 Conference Papers*. 1–9.
- [30] Lingjie Liu, Jiatao Gu, Kyaw Zaw Lin, Tat-Seng Chua, and Christian Theobalt. 2020. Neural sparse voxel fields. *Advances in Neural Information Processing Systems* 33 (2020), 15651–15663.
- [31] Tao Lu, Mulin Yu, Linning Xu, Yuanbo Xiangli, Limin Wang, Dahua Lin, and Bo Dai. 2024. Scaffold-gs: Structured 3d gaussians for view-adaptive rendering. In *Proceedings of the IEEE/CVF Conference on Computer Vision and Pattern Recognition*. 20654–20664.
- [32] Ben Mildenhall, Pratul P Srinivasan, Rodrigo Ortiz-Cayon, Nima Khademi Kalantari, Ravi Ramamoorthi, Ren Ng, and Abhishek Kar. 2019. Local light field fusion: Practical view synthesis with prescriptive sampling guidelines. *ACM Transactions on Graphics (TOG)* 38, 4 (2019), 1–14.
- [33] Ben Mildenhall, Pratul P Srinivasan, Matthew Tancik, Jonathan T Barron, Ravi Ramamoorthi, and Ren Ng. 2021. Nerf: Representing scenes as neural radiance fields for view synthesis. *Commun. ACM* 65, 1 (2021), 99–106.
- [34] Thomas Müller, Alex Evans, Christoph Schied, and Alexander Keller. 2022. Instant neural graphics primitives with a multiresolution hash encoding. *ACM transactions on graphics (TOG)* 41, 4 (2022), 1–15.
- [35] Jacob Munkberg, Jon Hasselgren, Tianchang Shen, Jun Gao, Wenzheng Chen, Alex Evans, Thomas Müller, and Sanja Fidler. 2022. Extracting triangular 3d models, materials, and lighting from images. In *Proceedings of the IEEE/CVF Conference on Computer Vision and Pattern Recognition*. 8280–8290.
- [36] Simon Niedermayr, Josef Stumpfegger, and Rüdiger Westermann. 2024. Compressed 3d gaussian splatting for accelerated novel view synthesis. In *Proceedings of the IEEE/CVF Conference on Computer Vision and Pattern Recognition*. 10349–10358.

[37] Ben Poole, Ajay Jain, Jonathan T Barron, and Ben Mildenhall. 2022. Dreamfusion: Text-to-3d using 2d diffusion. *arXiv preprint arXiv:2209.14983* (2022).

[38] Kerui Ren, Lihan Jiang, Tao Lu, Mulin Yu, Lining Xu, Zhangkai Ni, and Bo Dai. 2024. Octree-gs: Towards consistent real-time rendering with lod-structured 3d gaussians. *arXiv preprint arXiv:2403.17898* (2024).

[39] Samuel Rota Bulò, Lorenzo Porzi, and Peter Kortschieder. 2024. Revising densification in gaussian splatting. In *European Conference on Computer Vision*. Springer, 347–362.

[40] Johannes L Schonberger and Jan-Michael Frahm. 2016. Structure-from-motion revisited. In *Proceedings of the IEEE conference on computer vision and pattern recognition*. 4104–4113.

[41] Jianxiong Shen, Antonio Agudo, Francesc Moreno-Noguer, and Adria Ruiz. 2022. Conditional-flow nerf: Accurate 3d modelling with reliable uncertainty quantification. In *European Conference on Computer Vision*. Springer, 540–557.

[42] Jianxiong Shen, Adria Ruiz, Antonio Agudo, and Francesc Moreno-Noguer. 2021. Stochastic neural radiance fields: Quantifying uncertainty in implicit 3d representations. In *2021 International Conference on 3D Vision (3DV)*. IEEE, 972–981.

[43] Yuan Shen, Duygu Ceylan, Paul Guerrero, Zexiang Xu, Niloy J Mitra, Shenlong Wang, and Anna Fröststück. 2024. SuperGaussian: Repurposing Video Models for 3D Super Resolution. *arXiv preprint arXiv:2406.00609* (2024).

[44] Karen Simonyan and Andrew Zisserman. 2014. Very deep convolutional networks for large-scale image recognition. *arXiv preprint arXiv:1409.1556* (2014).

[45] Adam Tonderski, Carl Lindström, Georg Hess, William Ljungbergh, Lennart Svensson, and Christoffer Petersson. 2024. Neurad: Neural rendering for autonomous driving. In *Proceedings of the IEEE/CVF Conference on Computer Vision and Pattern Recognition*. 14895–14904.

[46] Matias Turkulainen, Xuqian Ren, Jaroslav Melekhov, Otto Seiskari, Esa Rahtu, and Juho Kannala. 2024. Dn-splatter: Depth and normal priors for gaussian splatting and meshing. *arXiv preprint arXiv:2403.17822* (2024).

[47] Chen Wang, Xian Wu, Yuan-Chen Guo, Song-Hai Zhang, Yu-Wing Tai, and Shi-Min Hu. 2022. Nerf-sr: High quality neural radiance fields using supersampling. In *Proceedings of the 30th ACM International Conference on Multimedia*. 6445–6454.

[48] Jianyi Wang, Zongsheng Yue, Shangchen Zhou, Kelvin C.K. Chan, and Chen Change Loy. 2024. Exploiting Diffusion Prior for Real-World Image Super-Resolution. (2024).

[49] Zhiru Wang, Shiyun Xie, Chengwei Pan, and Guoping Wang. 2024. SpecGaussian with Latent Features: A High-quality Modeling of the View-dependent Appearance for 3D Gaussian Splatting. In *Proceedings of the 32nd ACM International Conference on Multimedia*. 6270–6278.

[50] Zhengxue Wang, Zhiqiang Yan, and Jian Yang. 2024. Sgnet: Structure guided network via gradient-frequency awareness for depth map super-resolution. In *Proceedings of the AAAI Conference on Artificial Intelligence*, Vol. 38. 5823–5831.

[51] Haolin Xiong. 2024. *Sparsegs: Real-time 360° sparse view synthesis using gaussian splatting*. Master’s thesis. University of California, Los Angeles.

[52] Zhiwen Yan, Weng Fei Low, Yu Chen, and Gim Hee Lee. 2024. Multi-scale 3d gaussian splatting for anti-aliased rendering. In *Proceedings of the IEEE/CVF Conference on Computer Vision and Pattern Recognition*. 20923–20931.

[53] Ziyi Yang, Xinyu Gao, Yangtian Sun, Yihua Huang, Xiaoyang Lyu, Wen Zhou, Shaohui Jiao, Xiaojuan Qi, and Xiaogang Jin. 2024. Spec-gaussian: Anisotropic view-dependent appearance for 3d gaussian splatting. *arXiv preprint arXiv:2402.15870* (2024).

[54] Zeyu Yang, Hongye Yang, Zijie Pan, and Li Zhang. 2023. Real-time photorealistic dynamic scene representation and rendering with 4d gaussian splatting. *arXiv preprint arXiv:2310.10642* (2023).

[55] Yao Yao, Zixin Luo, Shiwei Li, Tian Fang, and Long Quan. 2018. Mvsnnet: Depth inference for unstructured multi-view stereo. In *Proceedings of the European conference on computer vision (ECCV)*. 767–783.

[56] Wang Yifan, Felice Serena, Shihao Wu, Cengiz Oztireli, and Olga Sorkine-Hornung. 2019. Differentiable surface splatting for point-based geometry processing. *ACM Transactions on Graphics (TOG)* 38, 6 (2019), 1–14.

[57] Youngho Yoon and Kuk-Jin Yoon. 2023. Cross-guided optimization of radiance fields with multi-view image super-resolution for high-resolution novel view synthesis. In *Proceedings of the IEEE/CVF Conference on Computer Vision and Pattern Recognition*. 12428–12438.

[58] Zehao Yu, Anpei Chen, Binbin Huang, Torsten Sattler, and Andreas Geiger. 2024. Mip-splatting: Alias-free 3d gaussian splatting. In *Proceedings of the IEEE/CVF Conference on Computer Vision and Pattern Recognition*. 19447–19456.

[59] Richard Zhang, Phillip Isola, Alexei A Efros, Eli Shechtman, and Oliver Wang. 2018. The unreasonable effectiveness of deep features as a perceptual metric. In *Proceedings of the IEEE conference on computer vision and pattern recognition*. 586–595.

[60] Zheng Zhang, Wenbo Hu, Yixing Lao, Tong He, and Hengshuang Zhao. 2024. Pixel-gs: Density control with pixel-aware gradient for 3d gaussian splatting. In *European Conference on Computer Vision*. Springer, 326–342.

[61] Zhe Zhang, Rui Peng, Yuxi Hu, and Ronggang Wang. 2023. Geomvsnet: Learning multi-view stereo with geometry perception. In *Proceedings of the IEEE/CVF conference on computer vision and pattern recognition*. 21508–21518.

[62] Zehao Zhu, Zhiwen Fan, Yifan Jiang, and Zhangyang Wang. 2023. FSGS: Real-Time Few-Shot View Synthesis using Gaussian Splatting. *arXiv:2312.00451* [cs.CV]